



**HAL**  
open science

## **AuCu/CeO<sub>2</sub> bimetallic catalysts for the selective oxidation of fatty alcohol ethoxylates to alkyl ether carboxylic acids**

Q. Gu, W.-H. Fang, R. Wischert, W-J Zhou, Carine Michel, M. Pera-Titus

► **To cite this version:**

Q. Gu, W.-H. Fang, R. Wischert, W-J Zhou, Carine Michel, et al.. AuCu/CeO<sub>2</sub> bimetallic catalysts for the selective oxidation of fatty alcohol ethoxylates to alkyl ether carboxylic acids. Chinese Journal of Catalysis, 2019, 10.1016/j.jcat.2019.10.017 . hal-02360384

**HAL Id: hal-02360384**

**<https://hal.science/hal-02360384>**

Submitted on 12 Nov 2019

**HAL** is a multi-disciplinary open access archive for the deposit and dissemination of scientific research documents, whether they are published or not. The documents may come from teaching and research institutions in France or abroad, or from public or private research centers.

L'archive ouverte pluridisciplinaire **HAL**, est destinée au dépôt et à la diffusion de documents scientifiques de niveau recherche, publiés ou non, émanant des établissements d'enseignement et de recherche français ou étrangers, des laboratoires publics ou privés.

# AuCu/CeO<sub>2</sub> bimetallic catalysts for the selective oxidation of fatty alcohol ethoxylates to alkyl ether carboxylic acids

Q. Gu,<sup>2‡</sup> W.-H. Fang,<sup>1†‡</sup> R. Wischert,<sup>1</sup> W.-J. Zhou,<sup>1\*</sup> C. Michel,<sup>2\*</sup> & M. Pera-Titus<sup>1\*</sup>

<sup>1</sup> *Eco-Efficient Products and Processes Laboratory (E2P2L), UMI 3464 CNRS-Solvay, 3966 Jin Du Road, Xin Zhuang Ind. Zone, 201108 Shanghai, China*

<sup>2</sup> *Univ Lyon, Ens de Lyon, CNRS UMR 5182, Université Claude Bernard Lyon 1, Laboratoire de Chimie, F69342 Lyon, France*

\* Corresponding authors: [wenjuan.zhou@solvay.com](mailto:wenjuan.zhou@solvay.com), [carine.michel@ens-lyon.fr](mailto:carine.michel@ens-lyon.fr), [marc.pera-titus-ext@solvay.com](mailto:marc.pera-titus-ext@solvay.com)

† Present address: *School of Chemical Science and Technology, Key Laboratory of Medicinal Chemistry for Natural Resource – Ministry of Education, Functional Molecules Analysis and Biotransformation, Key Laboratory of Universities in Yunnan Province, Yunnan University, 650091 Kunming, China*

‡ These authors contributed equal to the work

---

## Abstract

We describe in this work the preparation of a series of bimetallic Au-Cu catalysts supported over nanoceria for the direct oxidation of C<sub>12</sub>-C<sub>14</sub>-alcohol polyethyleneglycol ether with on average 7 ethyl oxide units (AEO7) to polyoxyethylene lauryl ether carboxylic acid (AECA6), using H<sub>2</sub>O<sub>2</sub> as an oxidant, under basic conditions. Different preparation methods have been used, including deposition-precipitation, incipient wetness impregnation and wet impregnation for engineering the interaction between Au, Cu and nanoceria. The structure of the bimetallic catalysts is discussed in detail on the basis of a refined characterization by XRD, HR-TEM, STEM-EDX-SDD, XPS and ICP-AES. The formation of a AuCu alloy over nanoceria at a Cu/Au molar ratio of 0.11 on Au allows a significant enhancement of the catalytic activity, resulting in an AECA6 yield up to 80% with a selectivity of 90%. The catalyst can be recycled and reused for at least 10 consecutive runs without apparent loss of activity. Detailed DFT calculations on Au, Cu and Au-Cu model alloys reveal a positive role of Cu on Au by favoring the adsorption of AEO7, H<sub>2</sub>O<sub>2</sub> and OH<sup>-</sup> on the catalyst surface compared to pure Au, as well as by reducing the energy barrier for H<sub>2</sub>O<sub>2</sub> cleavage. Isolated Cu sites on the Au-Cu alloy appear as crucial for enhancing the catalytic properties for AEO7 oxidation.

*Keywords:* Oxidation, hydrogen peroxide, alcohol ethoxylates, acid ethoxylate, supported nanoparticles, gold, copper, alloy, DFT

## 1. Introduction

Alcohol ether carboxylic acids (AECAs) are widely used as anionic surfactants in the oil and gas, home and personal care and industrial formulations because of their low viscosity, high foaming capacity and low harm to eyes and skin [1,2]. As of today, carboxymethylation of C<sub>n</sub>-alcohol polyethyleneglycol ethers using chloroacetic acid (i.e. Williamson's ether synthesis) is the main industrial route for the production of AECAs. However, this route is seriously constrained due to the use of excess amounts of toxic chloroacetic acid and the generation of sodium chloride as byproduct. Besides, nitroxyl radicals such as TEMPO can be used as catalysts for AECA production by the oxidation of alcohol ethoxylates (AEOs) with O<sub>2</sub> and nitric acid [3]. Besides the use of highly corrosive nitric acid, this route suffers from low selectivity towards AECAs, because large amounts of aldehydes and esters are formed.

As a greener alternative, noble metal catalysts have been regarded as a good option for the direct oxidation of AEOs to AECAs in aqueous, alkaline medium (pH 9-11), using either O<sub>2</sub> or H<sub>2</sub>O<sub>2</sub>, affording water as main byproduct [4]. As a rule, even if Pt and Pd catalysts can be *a priori* suitable for the aqueous oxidation of alcohols [5,6], these metals usually feature moderate selectivity, poor activity (<0.2 mmol.min<sup>-1</sup>.g<sub>Pt/Pd</sub><sup>-1</sup>), insufficient stability and deactivation by over-oxidation and metal leaching, discouraging industrial implementation [7]. Besides Pt and Pd catalysts, Au nanoparticles with small particle sizes (often <3 nm) have shown promising credentials for catalyzing alcohol oxidation reactions using O<sub>2</sub> and H<sub>2</sub>O<sub>2</sub> as an oxidant in the presence of a base [8-10].

The mechanisms behind alcohol oxidation reactions have been studied using computational tools [11-18]. On noble metals, it was found that adsorbed OH can assist C-H cleavage both from the -OH and the α-CH group. The first step of alcohol oxidation is always O-H cleavage followed by C-H cleavage from the α-CH group, generating the aldehyde. The next step is the addition of an

OH species, followed by a second C-H cleavage to form the carboxylic acid [11]. Surface hydroxyl species can be regenerated by O-O scission of H<sub>2</sub>O<sub>2</sub> and water, or by recombination of water and O<sub>2</sub>, closing the catalytic cycle [13,15]. To be active, Au catalysts require a basic environment, an effect that can be ascribed to the polarization of the water/Au interface induced by the adsorption of the anionic OH<sup>-</sup> and an easier desorption of the carboxylate product [18]. In addition to OH<sup>-</sup>-driven mechanisms, nanocrystalline ceria (or simply nanoceria) combined with Au nanoparticles are known to promote a catalytic mechanism for the base-free oxidation of 2-propanol driven by Ce<sup>3+</sup> and Au<sup>+</sup> species at the Au@ceria interface [19].

Alloying is often regarded as a useful strategy for promoting the activity of metal-supported catalysts, which can be rationalized by two main aspects [20,21]: (1) a ligand effect due to the change of chemical properties such as charge transfer between the metals, orbital rehybridization and lattice strain; and (2) an ensemble effect due to the change of the chemical composition, which alters the catalytic properties by providing different adsorption and active sites on the metal surface. Such effects can be used for designing surface and bulk alloys based on Au for conducting oxidation reactions. The addition of a second metal (*e.g.*, Pd and Pt) is known to enhance the catalytic activity and stability of Au nanoparticles [22,23]. In particular, the genesis of Pd monomers isolated by Au atoms on Pd-Au alloys can exert a considerable effect on the catalyst activity and selectivity for methanol and glycerol oxidation [17,24]. The role of isolated atoms was also studied in formic acid decomposition catalyzed by a Ni-Au alloy [25]. The authors found that isolated Ni destabilized the HCOO bidentate intermediate compared to pure Ni, decreasing the possibility of poisoning by HCOO species. This study illustrates the importance of isolated atoms with a catalytic role driven by the ensemble effect brought by Ni-Au sites.

The particle size, shape, crystal structure and electronic properties of Au nanoparticles can be conditioned to an important extent by doping with Cu [26]. Different Au-Cu cluster architectures

(*e.g.*, bulk alloy, Au-rich/Cu-rich, Cu-rich/Au-rich, core/shell) can be prepared, depending on the Au-Cu composition, the type of support, and the preparation method [27,28]. Supported Au-Cu formulations have shown high activity, selectivity and stability against sintering in CO oxidation [29,30], and in liquid-phase aerobic oxidation reactions with special emphasis on biobased reagents (*e.g.*, 5-hydroxymethylfurfural, HMF) [31-33]. Noteworthy, the promoting effect of Cu on Au catalysts for CO oxidation in the presence of O<sub>2</sub> has been confirmed by DFT calculations [34,35].

Despite the promising credentials of Au-based catalysts and alloys for alcohol oxidation, few examples have been reported for the oxidation of AEOs to AECAs. Clariant patented a very active and selective catalyst based on 0.1 wt% (Au/Pt 9:1) supported over CeO<sub>2</sub> for the aqueous oxidation of a series of AEOs in diluted conditions (5 wt%) and in the presence of a base (pH 11), using O<sub>2</sub> as oxidant [36]. The catalyst showed higher activity (x500) and selectivity (99% vs. 85-95%), compared to Pt and Pd catalysts, as well as improved stability against deactivation. Further studies by Prüsse and coworkers pointed out a relevant role of ceria on suppressing metal leaching by stabilizing Au nanoparticles, avoiding sintering [37,38]. We also reported a bimetallic AuPt/TiO<sub>2</sub> catalyst based on 0.1 wt% (Au/Pt 9:1), showing high catalytic activity and selectivity in the oxidation of C<sub>12</sub>-C<sub>14</sub>-alcohol polyethyleneglycol ether (AEO7) to polyoxyethylene lauryl ether carboxylic acid (AECA6) at 80 °C, using H<sub>2</sub>O<sub>2</sub> as an oxidant in the presence of a base [39]. Noteworthy, doping with Pt enhanced the catalyst stability against over-oxidation and sintering.

Pursuing out attempts in the preparation of stable catalysts for AEO oxidation, herein we report the preparation of bimetallic Au-Cu formulations over nanoceria for the oxidation of AEO7 to AECA6 at high concentrations (>20 wt%). The formulations were prepared by different methods, including deposition-precipitation, incipient wetness and wet impregnation. The preparation method, as well as the addition sequence of the Au and Cu precursors over nanoceria, exerts an important effect on the properties of the bimetallic catalysts. To mitigate mass transfer

effects ascribed to the high viscosity of concentrated AEO solutions, as well as foaming under air, the catalytic tests were conducted using H<sub>2</sub>O<sub>2</sub> as an oxidant. The ability of Cu for conditioning the structure of the catalysts will be discussed in detail on the basis of fine characterization by XRD, HR-TEM, STEM-EDX-SDD, XPS and ICP-AES form combined with DFT calculations.

## 2. Experimental

### 2.1. Materials

Gold (III) chloride trihydrate (HAuCl<sub>4</sub>·3H<sub>2</sub>O, J&K Chemical, ≥49.0%Au), copper(II) chloride dehydrate (CuCl<sub>2</sub>·2H<sub>2</sub>O, J&K Chemical, ≥99.0%), nanoceria (CeO<sub>2</sub>, Solvay, HSA20SP, 130 m<sup>2</sup>/g) and sodium borohydride (NaBH<sub>4</sub>, J&K Chemical, 98.0%) were used as received for preparing the supported metal catalysts. Polyoxyethylene lauryl ether (AEO7, Sasol), hydrogen peroxide (H<sub>2</sub>O<sub>2</sub>, Sinopharm, ≥30.0%) and sodium hydroxide (NaOH, Sinopharm, ≥96%) were used for carrying out the catalytic tests. Sodium chloride (NaCl, Sinopharm, 99.5%), sulfuric acid (H<sub>2</sub>SO<sub>4</sub>, Sinopharm, 95-98%), magnesium sulfate (MgSO<sub>4</sub>, Sinopharm, 98%) and dichloromethane (CH<sub>2</sub>Cl<sub>2</sub>, Sinopharm, 99.5%) were used for product treatment. CDCl<sub>3</sub> was used as NMR solvent. The different materials were used as received without any further purification or treatment.

### 2.2. Catalyst preparation

The bimetallic Au-Cu catalysts supported over nanoceria were prepared by different methods, including deposition-precipitation (DP), incipient wetness (IWI) and wet impregnation (WI). In the DP and IWI methods, the Au and Cu aqueous precursors were codeposited/coimpregnated using an aqueous solution of the Au and Cu precursors. In contrast, for the catalysts prepared by WI, the Au and Cu aqueous precursors were either coimpregnated, or impregnated in two sequential steps. All catalysts were reduced at different temperatures using an aqueous solution of NaBH<sub>4</sub>.

### 2.2.1. Deposition-Precipitation

In a typical preparation, 300 mL of an aqueous suspension containing 2.0 g of the nanoceria powder was adjusted to pH 10 by adding NaOH dropwise. In parallel, 350 mL of an aqueous solution containing 0.0408 g of  $\text{HAuCl}_4 \cdot 3\text{H}_2\text{O}$  and a given amount of  $\text{CuCl}_2 \cdot 2\text{H}_2\text{O}$  was adjusted to pH 10 by adding NaOH dropwise, and the solution was then added to the nanoceria suspension to favor the coprecipitation of both precursors. The pH of the resulting slurry was readjusted to 10 and then continuously stirred during 2 h. Later, 5 mL of an aqueous solution containing 0.13 g of  $\text{NaBH}_4$  was added dropwise either at room temperature or at 60 °C. The final catalysts were filtered, washed with deionized water until no chloride trace was detected using a  $\text{AgNO}_3$  test, and then freeze-dried under vacuum for 24 h.

Two catalysts were prepared by the DP method, which are hereinafter referred to as  $1\text{Au}(x\text{Cu})_{\text{DP\_RT}}$  and  $1\text{Au}(x\text{Cu})_{\text{DP\_60}}$  (nominal loadings: 1 wt% Au, x wt% Cu), where RT and 60 refer to reduction at either room temperature or 60 °C.

### 2.2.2. Incipient Wetness Impregnation

In a typical preparation, 0.0408 g of  $\text{HAuCl}_4 \cdot 3\text{H}_2\text{O}$  and a given amount of  $\text{CuCl}_2 \cdot 2\text{H}_2\text{O}$  were dissolved simultaneously in deionized water using a volume matching the pore volume of 2.0 g of nanoceria. The resulting solution was added dropwise to the nanoceria support under vigorous stirring until the entire liquid was absorbed, and the impregnated support was freeze-dried under vacuum for 24 h, calcined at 300 °C for 4 h either under an air flow [ $20 \text{ cm}^3(\text{STP})/\text{min}$ ], or under a 20%  $\text{H}_2/\text{Ar}$  flow [ $20 \text{ cm}^3(\text{STP})/\text{min}$ ].

Two coimpregnated catalysts were prepared by the IWI method, which are hereinafter referred to as  $1\text{Au}(x\text{Cu})_{\text{IWI\_Air}}$  and  $1\text{Au}(x\text{Cu})_{\text{IWI\_H}_2}$  (nominal loadings: 1 wt% Au, x wt% Cu).

### 2.2.3. Wet impregnation



Two Au and Cu precursor solutions were prepared by dissolving 0.0408 g of  $\text{HAuCl}_4 \cdot 3\text{H}_2\text{O}$  in 350 mL of deionized water, and a given amount of  $\text{CuCl}_2 \cdot 2\text{H}_2\text{O}$  in 350 mL of deionized water, respectively. Three impregnation methods were used:

- i) Coimpregnation of Au and Cu by adding a given volume of the Cu precursor solution to the Au precursor solution (350 mL), addition of the final solution to 20 mL of an aqueous suspension of 2.0 g of nanoceria under stirring, and continuous stirring of the resulting slurry for 1 h at room temperature. Then, dropwise addition of 5 mL of an aqueous solution containing 0.13 g of  $\text{NaBH}_4$  at room temperature, followed by filtration, washing with deionized water until no chloride trace detection using a  $\text{AgNO}_3$  test, and freeze-drying under vacuum for 24 h.
- ii) First, Au impregnation by adding the Au precursor solution (350 mL) to 20 mL an aqueous suspension of 2.0 g of nanoceria under stirring. Then, dropwise addition of 5 mL of an aqueous solution containing 0.13 g of  $\text{NaBH}_4$  at room temperature, followed by filtration, washing with deionized water until no chloride trace detection using a  $\text{AgNO}_3$  test, and freeze-drying under vacuum for 24 h. Subsequently, Cu impregnation by adding a given volume of the Cu precursor solution to the as-obtained catalyst and continuous stirring of the resulting slurry for 1 h at room temperature, followed by filtration, washing with deionized water until no chloride trace detection using a  $\text{AgNO}_3$  test, and freeze-drying under vacuum for 24 h.
- iii) The preparation procedure is similar to ii), but Cu was first impregnated on the nanoceria. After reduction, washing and drying, Au was impregnated on the Cu-catalyst.

For the sake of clarity, the nomenclature 1Au(xCu)\_WI, 1Au-xCu\_WI and xCu-1Au\_WI (nominal loadings: 1 wt%Au, x wt%Cu), is hereinafter used to refer to the bimetallic catalysts

prepared by wet impregnation using methods *i*, *ii* and *iii*, respectively. For comparison, pure 1Au\_WI and xCu\_WI catalysts were also prepared over nanoceria (nominal loadings: 1 wt%Au or x wt%Cu) by this method using the corresponding precursor solutions.

### 2.3. Catalyst characterization

Inductively Coupled Plasma Atomic Emission Spectroscopy (ICP-AES) was used to quantify the Au and Cu bulk content of the catalysts using a Thermo IRIS Intrepid II XSP atomic emission spectrometer. Before the measurements, the samples were dissolved using a HNO<sub>3</sub>/H<sub>2</sub>SO<sub>4</sub>/HF solution.

The phases present in the different catalysts were analyzed by powder X-ray diffraction (PXRD). The PXRD patterns were recorded on a Rigaku D/Max-2200/PC diffractometer provided with Cu-K $\alpha_{1+2}$  radiation ( $\lambda = 1.5418 \text{ \AA}$ ) and a beam voltage of 45 kV. The spectra were collected in the  $2\theta$  range 8-80° with a step size of 0.02°. The patterns were indexed using the Joint Committee on Powder Diffraction (JCPDS) database and interpreted using MDI JADE 5.0 software. The Scherrer equation was used to estimate the average size of the ceria nanoparticles from the XRD line broadening.

The textural properties of the catalysts were inspected by N<sub>2</sub> adsorption at 77 K using a Micrometrics Tristar II apparatus. The surface areas were calculated by the Brunauer-Emmett-Teller (BET) method in the relative pressure range  $0.05 < P/P_0 < 0.35$ , while the pore volumes were measured at  $P/P_0=0.99$ . The external surface was estimated using the t-plot method. Prior to the measurements, the catalysts were degassed at 150 °C for 3 h under vacuum (0.5 mbar).

The surface composition of the catalysts was analyzed by X-ray photoelectron spectroscopy (XPS) using a Thermo ESCALAB 250 spectrometer with monochromatic Al K $\alpha$  radiation ( $h\nu = 1486.6 \text{ eV}$ ). The spectra were recorded using an Al monochromated X-ray source (15 kV, 15 mA) with a pass energy of 30 eV (0.05 eV/step) for high resolution spectra, and a pass energy of 70 eV

(1 eV/step) for survey spectrum in hybrid mode and slot lens mode, respectively. The adventitious C1s binding energy (285.0 eV) was used as an internal reference.

Transmission electron microscopy (TEM) was used to measure average size and distribution of metal nanoparticles using a JEOL JEM 2100 microscope. The local composition of the catalysts was inspected by STEM-EELS/EDS using a 200 kV Tecnai F20 microscope equipped with a FEG electron gun, a STEM unit and an EDAX Optima T60 SDD-EDS spectrometer. The images were analyzed using EDAX Team microanalysis software and quantified using the Cliff-Lorimer method. Before the analysis, the given solid powder was directly dispersed over a holey carbon Cu or Co 400 mesh grid (Agar). The images were denoised using HyperSpy software.

#### **2.4. Catalytic activity measurements**

The protocol for conducting the catalytic tests for AEO7 oxidation was adapted from a previous study [39]. Briefly, 20 g of an aqueous solution of AEO7 (33 wt.%) was mixed with NaOH and the desired catalyst in a three-necked flask equipped with a magnetic stirrer, a cooling condenser and a double-rowed pipe, to give NaOH/AEO7 and AEO7/metal molar ratios of 1.1 and 432, respectively. Then the system was vacuumed and refilled with N<sub>2</sub> three times by switching the valve of the double-rowed pipe. Later on, the flask was refilled with N<sub>2</sub> at a flowrate of 200 mL(STP)/min, the mixture was heated to 80 °C for 5 min and aqueous H<sub>2</sub>O<sub>2</sub> (35 wt.%) was added using a syringe pump during 10 h (optimal dosing time) for a total reaction time of 16 h until a final H<sub>2</sub>O<sub>2</sub>/AEO7 molar ratio of 6.4 to discourage self-decomposition.

After the reaction, the mixture was centrifuged to separate the solution from the catalyst and an excess amount of HCl was added to neutralize the base and decrease the solubility of the organic compounds. The organic compounds were extracted using CH<sub>2</sub>Cl<sub>2</sub>, MgSO<sub>4</sub> was added as a desiccant to absorb water traces, and the solvent was then separated using a rotary evaporator. The concentration of the non-reacted AEO7 and the reaction products present in the organic phase were

analyzed by  $^1\text{H-NMR}$  and  $^{13}\text{C-NMR}$ . Mass balances were accurate to within 5% in all the catalytic tests. Control experiments in the absence of catalyst revealed that the reaction was difficult to proceed with very low AEO7 conversion (<10%).

In each experiment, the AEO7 conversion, and the selectivity, yield and turnover number (TON) to the different products ( $i$ ), were defined using the following expressions (eqs 1-4)

$$\text{AEO7 conversion} = \left(1 - \frac{n_{\text{AEO7}}}{n_{\text{AEO7}}^0}\right) \times 100 \quad (1)$$

$$\text{Yield}_i = \frac{n_i}{n_{\text{AEO7}}^0} \times 100 \quad (2)$$

$$\text{Selectivity}_i = \frac{n_i}{n_{\text{AEO7}}^0 - n_{\text{AEO7}}} \times 100 \quad (3)$$

$$\text{TON}(t)_i = \frac{n_i(t)}{M_{\text{Au}}} \times 100 \quad (4)$$

where  $n_i$  is the number of moles of product  $i$ , and  $M_{\text{Au}}$  is the number of moles of Au added into the reaction system.

Dedicated recyclability and reuse tests were conducted on the best catalytic formulation at 80 °C for 16 h at an initial AEO7 concentration of 33 wt% (in water) and initial AEO7/metal,  $\text{H}_2\text{O}_2/\text{AEO7}$  and  $\text{NaOH}/\text{AEO7}$  molar ratios of 432, 6.4 and 1.1, respectively.  $\text{H}_2\text{O}_2$  addition was carried out during 10 h.

## 2.5. Computational details

### 2.5.1. Method

All calculations were performed using the Density Functional Theory (DFT) with the Vienna ab initio simulation package (VASP 5.4.1) [40-42]. The Perdew-Burke-Ernzerhof form of Generalized Gradient Approximation (GGA-PBE) functional was applied to obtain the exchange and correlation terms [43], and were dispersion-corrected using the dDsC method [44]. Projector-

augmented wave (PAW) pseudo potentials were used with a cut-off energy of 400eV [45]. The electronic self-consistent convergence was set to  $1 \times 10^{-6}$  eV, while the ionic relaxation convergence was set to 0.02 eV/Å in geometric optimization. The numerical accuracy was set to the Normal.

The optimal conventional unit cell parameter for Au and Cu were computed at 4.14 Å and 3.62 Å respectively, in excellent agreement with experimental data for Cu (3.62 Å) and reasonable agreement for Au (4.08 Å) [46]. These unit cell parameters were used to build Au and Cu slabs. In the case of surface Au-Cu alloys, the slabs were built using the Au parameter. To describe the metal/water interface, the solvent was described using a Polarizable Continuum model based on the linearized Poisson-Boltzmann equation (PB) and incorporating the Debye-Hückel theory of ionic solutions to describe the counter-charge as a point charge distribution [47,48], as implemented by the Hennig and coworkers in the VASPsol package [49,50]. To improve the numerical stability, the cavitation energy was not included in the implicit solvent model, and the cavity surface tension was set to zero. The electric-field screening effect in the electrolyte solvent was described at a Debye length of 3.0 Å [51]. Considering that the (111) surface is the most exposed facet by the supported nanoparticles, Au(111) and Cu(111) were chosen to model the Au and Cu catalysts. Au(111) and Cu(111) surfaces were modeled by a mirror symmetric periodic slab of 5 layers using a p(4×4) unit cell. The symmetry was kept along the whole reaction path for both the surface and the adsorbates. The middle layer was set in bulk position while the other layers were allowed to relax. The use of a symmetric slab was found necessary for a charged slab to avoid spurious dipole interactions. The Brillouin zone was integrated using a 3×3×1 and 5×5×1 Monkhorst-Pack grid respectively on Au and Cu. A large vacuum layer of 35 Å was used to obtain a constant potential in the bulk solution. The surface AuCu alloy were modeled by substituting 1 or 2 surface Cu atoms on Au(111).

The search for transition states was accomplished using the Climbing Image Nudged Elastic Band Method (CI-NEB) [52], for which 8 images along the reaction path were generated by Opt'n

Path [53]. The transition state structures were refined with the quasi-Newton (QN) algorithm and confirmed by frequency calculations (1 imaginary frequency corresponding to the reaction coordinate for an asymmetric surface, 2 imaginary frequencies for the symmetric surface). Molecular species and ions in the solvent were all computed in a  $20 \times 20 \times 20 \text{ \AA}^3$  unit cell.

The Gibbs free energies were computed within the rigid rotator and harmonic approximation. Regarding the translational entropy, we linked the gas entropy to the solution entropy using the scaling relation introduced by Wertz [54] (see SI for further details).

### 2.5.2. *Modeling the influence of the basic environment on the catalyst*

Modeling a basic aqueous environment on the catalyst is challenging. In the first reports, the impact of a large amount of hydroxide anions,  $\text{OH}^-$ , was assumed to increase the coverage of adsorbed hydroxyl species on the catalyst surface [14]. These studies considered the adsorption of radical OH instead of anionic  $\text{OH}^-$  that would polarize the metal/water interface. Despite the relevance of charged nanoparticles, the role of electrons on adsorbed  $\text{OH}^-$  has often been neglected [55-57]. Some of us recently proposed an approach combining a negatively metallic charged surface with a counter charge described by the PB equation to take explicitly into account the role of electrons donated by anionic  $\text{OH}^-$  to the metal nanoparticle [18,58]. In each metal symmetric slab, two electrons were introduced from two chemisorbed  $\text{OH}^-$  anions to mimic the basic environment. In a nutshell, the presence of a high concentration of  $\text{OH}^-$  results in strong polarization of the catalyst/water interface, which modifies the catalytic activity and assists the desorption of the carboxylate product from the catalyst surface.

### 2.5.3. *Reactants and products: from bulk water to the metal/water interface*

To properly describe the reaction energy, the PCM approach to model the water solvent was complemented by microsolvation with the inclusion of few explicit water molecules. As shown by

Thapa et al. [59], in absence of explicit water molecules, the predicted pKa of AEO1 was overestimated by 8.78 units by comparison with the experimental pKa of AEO1. When using a single water molecule, this error decreases to 5.13 pKa units, while the inclusion of three water molecules is the minimum number allowing a proper calculation of the pKa with an error of 0.83 compared to the experimental value. Thus, we chose three water molecules to improve the solvation model of AEO (see Figure 1).

The initial microsolvation structure of AECO<sup>-</sup>, representing the corresponding acid/oxidation product of AECH<sub>2</sub>OH, was constructed by analogy with CH<sub>3</sub>COO<sup>-</sup>, i.e. with 6 water molecules around the -COO<sup>-</sup> group, since the 1D-RISM theory predicts an average number of 6 H-bonds formed by -COO<sup>-</sup> with water [60]. For OH<sup>-</sup>, four water molecules were used to solvate the anion to the complete first solvation shell of OH<sup>-</sup> [61]. The corresponding microsolvated structures are depicted in Figure 1. Upon transfer from bulk water to the metal surface, we considered that the microsolvation shell is strongly disrupted and is mainly suppressed by the interaction between the functional groups of the reactants or products and the metal surface. Even if microsolvation of surface intermediates is relevant, especially on the most oxophilic transition metals [62,63], we decided to avoid the over-complexity of combining surface alloying and surface microsolvation. Accordingly, reactants, products and intermediates were not microsolvated once adsorbed at the metal/water interface. The water molecules involved in the microsolvation shell were relocated into bulk water during the transfer of molecular and anionic species from water to the metal surface.

### 3. Results

Our research strategy was organized in three main stages. To start, we aim at finding an efficient bimetallic Au-Cu catalyst supported over nanoceria to perform the oxidation of AEO7 into AECA6 at high concentration (33 wt%) and using H<sub>2</sub>O<sub>2</sub> as an oxidant. After comparing

various preparation protocols for catalyst preparation (section 2.1), we selected the wet impregnation method and optimized the Au/Cu ratio on the formulation. We found a very efficient (section 2.2) and also stable catalyst (section 2.3). In the second stage, we conducted extensive characterization of the Au-Cu catalysts at variable Cu loading and found that the best formulation exposes a Au-Cu surface alloy (section 2.4). Finally, in the third stage, we built a surface model for the Au and Au-Cu alloy catalysts, and conducted a mechanistic study using periodic DFT calculations to rationalize the structure-activity relationship on a model Au-Cu alloy being representative of the experimental formulation (section 2.5).

### 3.1. Effect of the preparation method

To assess the promoting role of Cu on ceria-based Au-Cu formulations for AEO7 oxidation, a series of bimetallic Au-Cu catalysts with a nominal 1 wt%Au and 0.1 wt%Cu was prepared by deposition-precipitation, incipient wetness impregnation and wet impregnation. **Table 1** compiles the catalytic results obtained. In all cases, the presence of base (i.e. OH<sup>-</sup>) was necessary to activate the catalyst, matching earlier results on supported Au catalysts over Al<sub>2</sub>O<sub>3</sub>, TiO<sub>2</sub> and nanoceria [39]. Irrespective of the calcination protocol, the catalysts prepared by incipient wetness impregnation [i.e. 1Au(0.1Cu)\_IWI\_Air and 1Au(0.1Cu)\_IWI\_H2] display low activity for AEO7 oxidation with around 20% AECA6 yield at 89% AECA6 selectivity (entries 1 and 2). In contrast, the catalysts prepared by deposition-precipitation [i.e. 1Au(0.1Cu)\_DP\_RT and 1Au(xCu)\_DP\_60] (entries 3 and 4) and wet impregnation [i.e. 1Au(0.1Cu)\_WI] (entry 5) are more active, exhibiting in both cases almost 80% AECA6 yield with negligible formation of cleaved by-products. For comparison, we also prepared two monometallic 1Au\_WI and 1Cu\_WI catalysts by wet impregnation of the corresponding precursors over nanoceria with 1 wt% nominal loading. 1Au\_WI exhibits the formation of AECA6 with 95% selectivity and 49% yield (entry 6). The main by-product observed is the carboxylic acid issued from the cleavage of one EO unit in AEO7 (e.g.,



lauric acid). In contrast, 0.1Cu\_WI appears to be fully inactive (entry 7). Because of its simplicity and convenience, in the remainder of this study, the catalysts were prepared by the wet impregnation method.

Subsequently, we investigated the effect of the wet impregnation sequence of the Au and Cu aqueous precursors over nanoceria on the catalytic performance of the bimetallic Au-Cu catalysts for AEO7 oxidation (Figure 2). The catalysts prepared by sequential impregnation of the Au and Cu of precursors, i.e. 1Au-0.1Cu\_WI and 0.1Cu-1Au\_WI, display a similar performance compared to 1Au\_WI with 92-95% AEO6 selectivity and an AECA yield of 41% and 50%, respectively (TON = 184 and 180 mol AECA6 / mol Au). In contrast, the coimpregnated catalyst [1Au(xCu)\_WI] exhibits a much higher activity, with a yield and selectivity of 76% and 95%, respectively (TON = 366 mol AECA6 / mol Au). In light of these results, the 1Au(0.1Cu)\_WI catalyst prepared by coimpregnation will be used in the remainder of this study for further optimization of the catalytic performance.

### 3.2. Optimization of 1Au(xCu) formulation

To optimize the Cu loading, we prepared a series of coimpregnated 1Au(xCu)\_WI catalysts over nanoceria with a nominal Cu content in the range  $x = 0.01-1$  wt%. Figure 3 plots the results obtained for AEO7 oxidation over the different catalysts. The AEC6 yield shows a slight decline after coimpregnation of 0.01 wt%Cu compared to the yield measured on the parent 1Au\_WI (from 49% to ~42%), whereas the AECA6 selectivity keeps almost unchanged at 95%. The AEC6 yield increases dramatically with the Cu loading in the range 0.01-0.20 wt%Cu until a maximum value of 80% for 1Au(0.2Cu) at an AECA6 selectivity of 93%, whereas it decreases further at higher Cu loading until *ca.* 39% at 1 wt%Cu, being lower than the yield obtained on the parent 1Au\_WI (49%). In all cases, the AECA6 selectivity keeps almost unchanged in the range 92-95% ( $\pm 3\%$ ). Irrespective of the Cu content, the main by-product formed is the carboxylic acid resulting from the

cleavage of one EO unit in AEO7. The best catalytic formulations were thus 1Au\_0.1Cu\_WI and 1Au\_0.2Cu\_WI with a TON of 336 and 343 mol AECA6 / mol Au, respectively, after 16 h reaction.

### 3.3. Catalyst stability

Given the promising catalytic performance of 1Au(0.1Cu)\_WI for AEO7 oxidation, a stability study was conducted on this formulation for at least 10 consecutive runs without any catalyst pretreatment before reuse (Figure 4). For comparison, the stability of the parent 1Au\_WI was also explored. 1Au(0.1Cu)\_WI displays a high level of reuse during operation with an AEO6 yield and selectivity of about 80% and 92%, respectively. High stability is also observed for 1Au\_WI in 4 consecutive runs at a comparable AEO6 selectivity (by 91%), but showing a lower AEO6 yield (by 40%). Both catalysts exhibit a promoted stability compared to Au/Al<sub>2</sub>O<sub>3</sub> and Au/TiO<sub>2</sub>, which were also prepared by wet impregnation [39], demonstrating the benefits of nanoceria 1Au\_WI and 1Au(0.1Cu)\_WI. The use of Cu as promoter keeps the selectivity towards AECA6 and the catalyst stability, and promotes the catalytic activity. Interestingly, compared to AuPt/CeO<sub>2</sub> also prepared wet coimpregnation of the Au and Pt precursors, the addition of Pt is not accompanied by a promoting effect on the catalytic activity (see more details in ref. [39]).

### 3.4. Understanding the structure of 1Au(xCu)\_WI catalysts

The catalytic results presented above point out an enhanced activity and selectivity of coimpregnated 1Au(0.1Cu)\_WI and 1Au(0.2Cu)\_WI formulations over nanoceria for AEO7 oxidation with a clear optimal at 0.1-0.2 wt%Cu nominal loading. In light of these results, we explored in more detail the structure and relative distribution of Au and Cu in the 1Au(0.1Cu)\_WI formulation.

#### 3.4.1. Textural properties

The textural properties of the different 1Au(xCu)\_WI formulations were measured by N<sub>2</sub> adsorption/desorption at -196 °C. **Table 2** (columns 4-6) list the BET specific surface area, total pore volume and average pore size of the formulations as a function of the Cu loading. In all cases, the N<sub>2</sub> adsorption isotherms (not shown) exhibit a S-shape pattern with a hysteresis loop in the P/P<sub>0</sub> range 0.7-1.0, which is indicative of the presence of mesopores with an average size of 8 nm in the nanoceria support. The specific surface area and pore volume keep almost unchanged after impregnation of the metal phase at about 125-130 m<sup>2</sup>/g and 0.31-0.32 cm<sup>3</sup>/g (**Table 2**), respectively, which are very similar to the values measured on the parent nanoceria support.

#### 3.4.2. Structural properties

The XRD patterns of the different 1Au(xCu)\_WI formulations exhibit the characteristic patterns attributed to fluorite-type CeO<sub>2</sub> (**Figure S1**). The average particle size of the CeO<sub>2</sub> nanoparticles falls in the range 5.8-7.1 nm as inferred by Scherrer equation applied to the (111) reflection. This size agrees well with the values measured on the precalcined CeO<sub>2</sub>-HS at 300 °C by XRD (5.6 nm, XRD) and HR-TEM (7.0 nm) (**Figure 5**). It is also worth mentioning that no additional reflections ascribed to Au (2-theta= 38.5°, 44.3°, 64.5°, JCPDS 04-0784), Cu<sub>2</sub>O (2-theta= 29.5°, 37°, 42.5°, JCPDS 05-0667) or CuO (2-theta= 33°, 35°, 38.5°, JCPDS 05-0937) are visible, which can be explained by the very low metal loading (max. 2 wt%), as well as to the small particle size of Au nanoparticles (≤ 3 nm).

The inspection of 1Au\_WI, 1Au(0.1Cu)\_WI and 1Au(1Cu)\_WI by HR-TEM (**Figure 5**) and STEM-EDS-SDD (**Figure 6**) confirms the genesis of very small Au nanoparticles (average size about 2-3 nm) on the different catalysts with an intimate interaction between Au and Cu in 1Au(0.1Cu)\_WI and 1Au(1Cu)\_WI at the level of spatial resolution of the cartography. Noteworthy, despite the low contrast between ceria and Au nanoparticles, the particle size of Au nanoparticles does not show an apparent change with the Cu loading and is similar to that observed

for monometallic 1Au\_WI. Besides, Cu is also found over nanoceria far apart from Au nanoparticles, especially at higher Cu loading.

Overall, these observations point out that the difference in catalytic activity between the different 1Au(xCu)\_WI formulations is not attributed to a variable Au dispersion or a variable particle size of Au nanoparticles, but to a promoting effect of Cu on Au. Indeed, the catalytic activity for AEO7 oxidation was found to keep unchanged with the Au particle size in the range 2-4 nm for Au/Al<sub>2</sub>O<sub>3</sub> and Au/TiO<sub>2</sub> (1 wt% Au) [39].

### 3.4.3. Structural properties

Figure 7 and Figure S2 plot the deconvoluted XPS spectra of the Au4f, Cu2p and Ce3d core levels for the pure 1Au\_WI and bimetallic 1Au(0.1Cu)\_WI formulations after reduction. Table 2 lists the binding energies (BEs) for the main bands (columns 7 and 8). The deconvoluted Ce3d core-level spectra could be assigned to eight spin-orbit coupling levels corresponding to the 3d<sub>5/2</sub> (*v*) and 3d<sub>3/2</sub> (*u*) states. The *v* components show binding energies (BE) at 879.6-880.1 eV (*v*<sub>0</sub>), 881.6-882.1 eV (*v*), 883.4-883.9 eV (*v*'), 888.0-888.5 eV (*v*'') and 897.6-898.1 eV (*v*'''), while the *u* components show BEs at 895.8-896.4 eV (*u*<sub>0</sub>), 900.0-900.2 eV (*u*), 901.8-902.2 eV (*u*'), 906.2-907.1 eV (*u*'') and 915.8-916.5 eV (*u*''') [64-66]. These components match the values measured on the deconvoluted XPS spectrum of the parent nanoceria support. The *v*' and *u*' components point out the presence of Ce<sup>3+</sup> in the first layers of the ceria nanoparticles and the relative amount of Ce<sup>3+</sup> does not change substantially after metal impregnation.

The XPS spectra of the Au4f core level for the 1Au(0.1Cu)\_WI formulations exhibit a main band centered in the range 83.5-84.1 eV (Au 4f<sub>7/2</sub>) that is consistent with metallic Au<sup>0</sup> (Figure 7A) [67,68]. Most of the BEs are lower than the BE of bulk Au (*ca.* 84 eV), which is indicative of a lower coordination of Au atoms on Au nanoparticles [69]. The formulations with intermediate Cu loading, i.e. 1Au(0.06Cu)\_WI, 1Au(0.10Cu)\_WI and 1Au(0.25Cu)\_WI, display a shift of the BE to

lower values. This observation can be explained by two main reasons: (1) a smaller particle size of Au nanoparticles as reported in previous studies on supported Au catalysts [33], and (2) an electron transfer from Cu to Au atoms, since Au is more electronegative than Cu, according to Pauling's electronegativity table [70]. However, the Cu2p<sub>3/2</sub> and Cu2p<sub>1/2</sub> levels do not shift to higher BEs, which means that the second interpretation does not apply to our case. Finally, a small shoulder is also visible in the 84.7-85.4 eV region, which can be assigned to oxidized Au<sup>+</sup> and Au<sup>3+</sup> species.

The XPS spectra of the Cu 2p core level for the 1Au(xCu)\_WI formulations display a characteristic spin-orbit doublet that can be assigned to the Cu2p<sub>3/2</sub> and Cu2p<sub>1/2</sub> components (Figure 7B). The Cu 2p peak is only visible when the Cu loading is higher than 0.1 wt%. Each component can be deconvoluted into a main species with a band centered at 932.4 ± 0.1 eV that can be attributed to Cu<sup>+</sup> and/or Cu<sup>0</sup> [71,72]. Noteworthy, this BE is only slightly lower than the value commonly accepted for bulk Cu (932.7 eV) and approaches the BE reported on small Cu clusters [73]. In view of this observation, we can attribute the lower BEs for the Au 4f<sub>7/2</sub> core level of 1Au(0.06Cu)\_WI, 1Au(0.10Cu)\_WI and 1Au(0.25Cu)\_WI to an electron transfer from Cu to Au atoms (*vide supra*). The weak Cu 2p signal precludes the identification of Cu<sup>2+</sup> species by deconvolution or from the presence of characteristic shake-up bands centered at 943.0 eV and 963.5 eV (not shown in the deconvolution). However, since Cu<sup>2+</sup> is known to undergo reduction under X-ray irradiation in ultra-high vacuum, the presence of Cu<sup>2+</sup> on the catalyst surface cannot be ruled out [74].

The Au and Cu weight loading measured by ICP-AES on 1Au(0.1Cu)\_WI, 1Au(0.2Cu)\_WI and 1Au(1Cu)\_WI after reduction are all close to the nominal values, whereas slight excess is observed for 1Au(0.01Cu)\_WI and 1Au(0.05Cu)\_WI (Table 2, columns 2 and 3). The different 1Au(xCu)\_WI catalysts show (Cu/Au)<sub>b</sub> bulk ratios in the range 0.077-3.33 on the nanoceria surface (Table 2, column 9). We also measured the (Cu/Au)<sub>b</sub> bulk ratio on the Au nanoparticles by STEM-

EDX-SDD using the Cliff-Lorimer method for 1Au(0.1Cu)\_WI and 1Au(1Cu)\_WI (Table 2, column 9). The surface analysis reveals a preferential location of *ca.* 35% of surface Cu interacting with Au nanoparticles for 1Au(0.1Cu)\_WI, resulting in a  $(\text{Cu}/\text{Au})_b$  bulk ratio of 0.11 on the Au surface. The percentage of surface Cu interacting with Au nanoparticles is, on average, lower for 1Au(1Cu)\_WI (about 15%), resulting in a  $(\text{Cu}/\text{Au})_b$  bulk ratio of about 0.46 on the Au surface. Finally, the surface Cu/Au molar ratios [i.e.  $(\text{Cu}/\text{Au})_s$ ] were measured by XPS are much higher than the corresponding bulk ratios measured by ICP-AES and STEM-EDX-SDD (Table 2, column 10). This observation points out partial Cu segregation on the catalyst surface. The enrichment by Cu on the catalyst surface is similar for 1Au(0.1Cu)\_WI and 1Au(0.2Cu)\_WI with a  $(\text{Cu}/\text{Au})_s$  surface ratio about 2.1. In contrast, 1Au(1Cu)\_WI with a higher Cu loading displays a  $(\text{Cu}/\text{Au})_s$  surface ratio of 5.0. This observation can be explained by a higher Cu dispersion on nanoceria far from the Au nanoparticles at higher Cu loadings, as well as by partial encapsulation / penetration of Au nanoparticles in nanoceria. Even if we are unable to discern between bulk and surface Au-Cu alloys, we can safely assume that the Cu concentration on the Au nanoparticles is low.

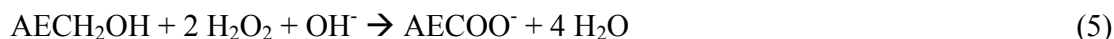
#### **4. Discussion: nature of Cu species and role on the catalytic activity**

The results presented in the section above point out the formation of Au-Cu alloys over nanoceria using the wet coimpregnation method of the Au and Cu precursors. Irrespective of the type of alloy generated, the  $(\text{Cu}/\text{Au})_s$  molar ratio of the Au-Cu alloys for 1Au(0.1Cu)\_WI should be about 0.11 (Table 2, column 9). In light of this result, we built different Au-Cu surfaces and conducted a complete DFT study to rationalize the promoting effect of Cu on the catalytic activity of 1Au(0.1Cu)\_WI for the oxidation of ethoxylated alcohols.

##### **4.1. Modeling the Au-Cu surface**

Under the premise of low Cu on the Au surface, we chose a simplified pure Au bulk for modeling Au-Cu alloys. Overall, two general forms of Au-Cu alloy were modeled: (1) mono alloy, which represents a single Cu atom surrounded by Au, where one Au atom of the Au surface is substituted by one Cu atom; and (2) dimer alloy, which represents aggregated Cu in the Au alloy, where two neighboring Au atoms are exchanged by two Cu atoms. The configuration of both alloys is depicted in [Figure 8](#).

We modeled the metallic surface in basic condition as a negatively charged surface (see details in refs. [\[18,67\]](#)). Using this model, we studied the complete oxidation path of AEO1 (used as a model of AEO7) to acetate in basic environment (eq 1) over pure Au, pure Cu, Au-Cu mono alloy, and Au-Cu dimer alloy. In the following, AEO1 will be expressed as AECH<sub>2</sub>OH, while the corresponding aldehyde and acid will be expressed as AECHO and AECO<sub>2</sub>H, respectively. Using these definitions, the overall reaction writes:



#### 4.2. Catalytic cycle for AECH<sub>2</sub>OH oxidation

[Figure 9](#) represents the catalytic cycle for AECH<sub>2</sub>OH oxidation with H<sub>2</sub>O<sub>2</sub>, whereas the corresponding Gibbs free energy profiles are plotted in [Figure 10](#). The structure of the reactants, products and intermediates on the different metals are represented in [Figure S3-S6](#). More details can be found in the Computational Details section.

The oxidation mechanism of AECH<sub>2</sub>OH by H<sub>2</sub>O<sub>2</sub> is analogous to that found for the oxidation of aliphatic alcohols by O<sub>2</sub> in presence of water [\[11,14,18\]](#). To start, 1 AECH<sub>2</sub>OH and 2 H<sub>2</sub>O<sub>2</sub> molecules from the bulk liquid phase (1) are adsorbed on the negatively charged surface. In parallel, 1 OH<sup>-</sup> is chemisorbed on a neutral surface, resulting in OH<sup>\*</sup> chemisorbed on a negatively charged surface (in blue) (2, indicated by a dashed box in [Figure 9](#)). The first stage (A –

*Adsorption*) ends with all reactants adsorbed separately. Then, we enter into the second stage (B – *H<sub>2</sub>O<sub>2</sub> activation*), where 2 H<sub>2</sub>O<sub>2</sub>\* is cleaved to 4 OH\* (labeled in red). The third stage (C – AECH<sub>2</sub>OH oxidation) corresponds to the oxidation of AECH<sub>2</sub>OH\* (4) into AE<sub>2</sub>COOH\* (8). The cycle closes by the last stage (D – desorption), consisting of the deprotonation of AE<sub>2</sub>COOH\* (8) to AE<sub>2</sub>COO\* (9) and its subsequent desorption in water under its anionic form, AE<sub>2</sub>COO<sup>-</sup> (10), regenerating an uncharged slab. In what follows, we will discuss all steps in detail and compare the activity predicted for different model of Au, Au-Cu and Cu catalysts.

#### 4.2.1. Stage A – Adsorption

Au and Cu show a contrasting behavior when adsorbing OH<sup>-</sup> on the neutral pristine (111) surface, resulting in a OH\* species on a negatively charged surface (Table 3). On Cu, OH<sup>-</sup> is preferentially adsorbed on the *fcc* sites with an adsorption Gibbs Free energy of -30 kJ/mol at 80 °C, while on Au, OH<sup>-</sup> adsorbs very weakly on Au-Au bridge sites with  $\Delta G_{\text{ads}} = 6$  kJ/mol. On Au-Cu alloys, OH<sup>-</sup> prefers to adsorb on Au-Cu or Cu-Cu bridge sites with an adsorption Gibbs Free energy of -37 kJ/mol and -84 kJ/mol for the Au-Cu mono and dimer alloys, respectively. These results point out that Cu atoms embedded in an Au matrix strongly stabilize OH\*, in particular in the case of the dimer alloy.

The H<sub>2</sub>O<sub>2</sub> adsorption energies and structures in basic media do not depend on the nature of the metal surface (Figure S7, Table 3), while the adsorption of AECH<sub>2</sub>OH is slightly more sensitive (Figure S8, Table S3). It is worth noting that the alloys always adsorb the species involved in the reaction more strongly than the monometallic surfaces, especially OH<sup>-</sup> and AECH<sub>2</sub>OH, which may facilitate the reaction compared to the pure metals.

#### 4.2.2. Stage B – H<sub>2</sub>O<sub>2</sub> activation



$\text{H}_2\text{O}_2^*$  is activated at the very beginning of the cycle to provide a source of  $\text{OH}^*$ . The activation of a second  $\text{H}_2\text{O}_2^*$  molecule is also required (see eq 1) to generate 4  $\text{OH}^*$  species in total and fulfill the oxidation of 1  $\text{AECH}_2\text{OH}^*$  to 1  $\text{AECOOH}^*$ . We consider here that the activation of the second  $\text{H}_2\text{O}_2^*$  occurs readily after the activation of the first  $\text{H}_2\text{O}_2^*$  as shown in **Figure 10** with the same transition state  $\text{TS}(\text{HO}-\text{OH})$ .

The highest barrier is observed for Au (36 kJ/mol), along with the longest O-O bond in the  $\text{TS}(\text{HO}-\text{OH})$  (1.80 Å) (**Figure 10**). On pure Cu,  $\text{H}_2\text{O}_2^*$  dissociation is much easier, with a barrier of only 10 kJ/mol and a relatively short O-O bond in the  $\text{TS}(\text{HO}-\text{OH})$  (1.60 Å). When Cu is available in the alloy,  $\text{H}_2\text{O}_2^*$  prefers to adsorb on Cu atoms (*vide supra*). In line with the more facile dissociation on the pure metal, the alloying Cu atom facilitates the dissociation of  $\text{H}_2\text{O}_2^*$  with a barrier of 18 kJ/mol and 6 kJ/mol on the Au-Cu mono and dimer alloys, respectively, with a short O-O bond in the  $\text{TS}(\text{HO}-\text{OH})$  (1.65 Å on mono alloy, 1.71 Å on dimer alloy).

#### 4.2.3. Stage C – $\text{AECH}_2\text{OH}$ oxidation

Assisted by  $\text{OH}^*$  as proton acceptor,  $\text{AECH}_2\text{OH}$  oxidation first goes through an O-H cleavage pathway from  $\text{AECH}_2\text{OH}^*$  (4) to  $\text{AECH}_2\text{O}^*$  (5) in a non-activated process (no TS could be located), consuming 1  $\text{OH}^*$  and generating 1  $\text{H}_2\text{O}$ , followed by  $\alpha$ -C-H cleavage from  $\text{AECH}_2\text{O}^*$  (5) to  $\text{AECHO}^*$  (6), again consuming 1  $\text{OH}^*$  and generating a 2<sup>nd</sup>  $\text{H}_2\text{O}$  molecule. The  $\alpha$ -C-H cleavage is still quite easy on Au with  $\text{OH}^*$  as a proton acceptor, with a small barrier [i.e.  $\text{TS}(\text{C}-\text{H})$ ] of 27 kJ/mol (**Figure 10**), which is in line with previous works where the barrier was found in a range of 12-64 kJ/mol for ethanol oxidation [11]. However, the  $\text{TS}(\text{C}-\text{H})$  barrier becomes larger when  $\text{AECH}_2\text{OH}^*$  reacts on Cu (114 kJ/mol), which is also in line with the value of 159 kJ/mol reported by Zuo et al. [16] After the generation of the aldehyde  $\text{AECHO}^*$  (6) from  $\text{AECH}_2\text{O}^*$  with  $\text{OH}^*$  (5), this step is followed by the addition of  $\text{OH}^*$ , generating the hydroxyalkoxy  $\text{AECHOOH}^*$  (7). This unstable intermediate undergoes barrierless reaction (abstraction of the labile  $\alpha$  C-H) with

a 4<sup>th</sup> OH\* to yield the carboxylic acid AECOOH\* (8) and a 3<sup>rd</sup> molecule of H<sub>2</sub>O. Finally, in basic and oxidative media, AECOOH\* (8) is not stable and will react with a 5<sup>th</sup> OH\* to generate AECOO\* (9) and a 4<sup>th</sup> molecule of H<sub>2</sub>O.

On pure metals, the limiting barrier of this stage C is the  $\alpha$ -C-H cleavage and is simply defined as the difference between AECH<sub>2</sub>O\* (5) and TS(C-H). This is not the case on alloys, as OH\* is very stable on Au-Cu alloys, displaying a *fcc* configuration in the presence of 2 Cu atoms as shown in [Figure S6](#). Then, state (4) with 5 OH\* in total becomes more stable than state (5), which includes 3 OH\* in a separated slab and 1 OH\* co-adsorbed with AECH<sub>2</sub>O\* limiting the interactions with Cu (see [Figure S6](#)). Thus, the overall limiting barrier of stage C for those alloys comes from the difference between (4) and TS(C-H) as shown in [Figure 10](#). In addition, this barrier is much larger than on Au (70 kJ/mol and 134 kJ/mol on the Au-Cu mono and dimer alloy, respectively). Since the OH\* stabilization is much stronger on the dimer alloy, the overall barrier of the  $\alpha$ -C-H cleavage is considerably increased, inhibiting the catalytic activity of this type of sites.

#### 4.2.4. Stage D – AECOO\* desorption

In basic aqueous environment, the desorbed molecule is AECOO<sup>-</sup> rather than AECOOH. [Table 3](#) lists the desorption energies of AECOO\* and H<sub>2</sub>O\*. AECOO\* desorption from the metal surface to AECOO<sup>-</sup> into bulk water is difficult for pure Cu and for the Au-Cu alloys, but becomes easier for Au. This observation is in line with the weaker adsorption of OH<sup>-</sup> on Au, compared to the other metal surfaces (*vide supra*). H<sub>2</sub>O\* desorption is not sensitive to the nature of the metal and proceeds fast for all metals and alloys. In a nutshell, desorption is rather easy for all catalysts in basic environment. In agreement with our previous work on the effect of the base on the alcohol oxidation [\[10\]](#), the desorption step is quite difficult for all metals and alloys in neutral environment ([Figure S9](#)), with a desorption barrier in a range of 126-325 kJ/mol as shown in [Table S1](#). The

strong adsorption of AECOO\* poisons all catalysts, thus preventing the oxidation of AECH<sub>2</sub>OH in neutral environment.

#### 4.2.5. Overall Pathway: Implications for AECH<sub>2</sub>OH oxidation

We collected the main barriers and energetic spans [75], as well as the rate-determining intermediate and transition state for each model catalytic surface (Figure 10, Table 4). The energetic span is large on pure Cu (114 kJ/mol), and slightly smaller on pure Au (105 kJ/mol). On Cu, this span is controlled by the barrier for cleavage of the  $\alpha$ -C-H bond. This barrier is much lower on Au (27 vs. 114 kJ/mol, *vide supra*) and the rate-determining transition state is defined by TS(HO-OH). On the Au-Cu alloys, the rate-determining transition state is again the  $\alpha$ -C-H cleavage, whereas the rate-determining intermediate is the preceding state (4) because of the increased stability of OH\*, as discussed earlier. On the dimer alloy, the energetic span is larger (134 kJ/mol) than on the pure metals, but it is strongly reduced for the mono alloy (70 kJ/mol). This implies that Cu dimer sites in Au-Cu alloys might be poisoned by OH\*, while isolated Cu sites show strongly enhanced reactivity. The predicted catalytic activity for complete AECH<sub>2</sub>OH oxidation is consistent with the experimental results in Figure 2: pure Cu is found inactive, Au shows moderate activity, and alloys with a lower Cu/Au bulk ratio (0.11, Table 2) perform the best. Alloys with higher Cu show reduced activity compared to pure Au. Assuming that in such a case the formation of Cu dimer sites is more probable, the predicted activity is again consistent with the experiments.

## Conclusion

In this study, we prepared a series bimetallic Au-Cu catalysts supported over nanoceria for the direct oxidation of C<sub>12</sub>-C<sub>14</sub>-alcohol polyethyleneglycol ether with on average 7 ethyl oxide units (AEO7) to polyoxyethylene lauryl ether carboxylic acid (AECA6), using H<sub>2</sub>O<sub>2</sub> as an oxidant and a

base. The formation of a AuCu alloy over nanoceria at a Cu/Au molar ratio of 0.11 on Au allows a significant enhancement of the catalytic activity, resulting in an AECA6 yield up to 80% with a selectivity of 90%. The catalyst could be recycled and reused for at least 10 consecutive runs without apparent loss of activity.

The promoting effect of Cu on Au could be rationalized using DFT calculations with AECH<sub>2</sub>OH as model for AEO7. In basic medium, Cu shows poor ability for oxidizing AECH<sub>2</sub>OH due to the difficulty in breaking the  $\alpha$ -C-H bond. In contrast,  $\alpha$ -C-H cleavage is easy on Au. When a Au atom is substituted by Cu (“mono alloy”, containing isolated Cu sites), a higher activity is predicted for AECH<sub>2</sub>OH oxidation: (i) isolated Cu sites on Au favor the adsorption of the reactants, compared to pure metals; (ii)  $\alpha$ -C-H cleavage is much easier, compared to pure Cu; and (iii) H<sub>2</sub>O<sub>2</sub> activation is also promoted compared to Au. The net effect is a strongly reduced energetic span, translating in higher catalytic activity, compared to pure Au and Cu. On the other hand, a higher density of Cu atoms leads to overstabilization of the intermediates, resulting in a much higher energetic span, compared to pure metals and alloys containing low Cu loading. In conclusion, isolated Cu sites on the Au-Cu appear as crucial for enhancing the catalytic properties for AEO7 oxidation to AECA6, which can be experimentally achieved at low Cu loading (0.1-0.2 wt%Cu).

## **Associated Content**

**Supporting Information.** XRD patterns of 1Au(xCu)\_WI formulations as a function of the Cu loading; deconvoluted XPS spectra of the Ce 3d core level for 1Au(xCu)\_WI formulations; structures involved in AECH<sub>2</sub>OH oxidation on p(4×4) Au(111), Cu(111), mono(111) and dimer(111) surfaces in basic environment; transition state of HOOH cleavage on Au(111), Cu(111), mono(111) and dimer(111) surfaces; transition state of  $\alpha$ -C-H cleavage from AECH<sub>2</sub>O to AECHO on Au(111), Cu(111), mono(111) and dimer(111) surfaces; free energy profile for

AECH<sub>2</sub>OH oxidation at 80 °C catalyzed by Au(111), Cu(111), mono(111) and dimer(111) in neutral environment; computed barriers of A-D stages, catalytic energetic span, free energy of reaction, rate-determining intermediate and rate-determining step of the complete AECH<sub>2</sub>OH oxidation reaction catalyzed by Au(111), Cu(111), mono(111) and dimer(111) in basic environment at 80 °C.

## **Acknowledgements**

W-J. Zhou gratefully acknowledges the Shanghai Youth Top-Notch Talent development program. The authors would like to express their gratitude to CNRS, Solvay, the SYSPROD project and AXELERA Pôle de compétitivité (PSMN Data Center) for funding. The authors also thank CINES in Montpellier, TGCC in Grenoble (project 609, GENCI/CT8), and PSMN in Lyon for CPU time and assistance. Dr. Eric Leroy from ICMPE-CMTR (UMR 7182 CNRS) is acknowledged for conducting the STEM-EDS-SDD analyses and fruitful discussion.

## **Abbreviations**

AECA, polyoxyethylene lauryl ether carboxylic acid; AECH<sub>2</sub>OH, 2-methoxyethan-1-ol; AECHO, 2-methoxyacetaldehyde; AECOOH, 2-methoxyacetic acid; AEO7, C<sub>12</sub>-C<sub>14</sub>-alcohol polyethyleneglycol ether; BE, binding energy; BET, Brunauer Emmett Teller; DFT, density functional theory; DP, deposition-precipitation; D<sub>p</sub>, average pore size; HMF, 5-hydroxymethylfurfural; HR-TEM, high-resolution transmission electron microscopy; ICP, inductively coupled plasma; IWI, incipient wetness impregnation; S<sub>BET</sub>, specific surface area; TEMPO, (2,2,6,6-tetramethylpiperin-1-yl)oxyl; STEM, scanning transmission electron microscopy; TON, turnover number; V<sub>p</sub>, porous volume; WI, wet impregnation; XPS, X-ray photoelectron spectroscopy; XRD, X-ray diffraction.

## References

- (1) W. W. Schmidt, D. R. Durante, R. Gingell, J. W. Harbell, *J. Am. Oil Chem. Soc.* 74 (1997) 25-31.
- (2) N. M. van Os, *Nonionic Surfactants: Organic Chemistry, Surfactant Science Series*, vol. 72, Marcel Dekker: NY, 1998.
- (3) H. E. Fried, US 5,162,579, 1992.
- (4) S. Zlatanov, K. Laskaridis, A. Sagredos, *Grasas y Aceites* 60 (2009) 360-366.
- (5) R. A. Sheldon, H. van Bekkum, *Fine Chemicals through Heterogeneous Catalysis*, Wiley-VCH, Weinheim, 2001.
- (6) M. Besson, P. Gallezot, *Catal. Today* 57 (2005) 127-141.
- (7) A. Abad, C. Almela, A. Corma, H. Garcia, *Tetrahedron* 62 (2006) 6666-6672.
- (8) G. J. Hutchings, *Chem. Commun.* (2008) 1148-1164.
- (9) A. S. K. Hashmi, G. J. Hutchings, *Angew. Chem. Int. Ed* 45 (2006) 7896-7936.
- (10) C. Della Pina, E. Falletta, M. Rossi, *Chem. Soc. Rev.* 41 (2012) 350-369.
- (11) B. N. Zope, D. D. Hibbits, M. Neurock, R. J. Davis, *Science* 330 (2010) 74-78.
- (12) C. Shang, Z-P. Liu, *J. Am. Chem. Soc.* 133 (2011) 9938-9947.
- (13) S. Chibani, C. Michel, F. Delbecq, C. Pinel, M. Besson, *Catal. Sci. Technol.* 3 (2013) 339-350.
- (14) D. D. Hibbits, M. Neurock, *J. Catal.* 299 (2013) 261-271.
- (15) T. Sheng, W. Lin, C. Hardacre, P. Hu, *J. Phys. Chem. C* 118 (2014) 5762-5772.
- (16) Z-J. Zuo, L. Wang, P-D. Han, W. Huang, *Int. J. Hydrogen Energy* 39 (2014) 1664-1679.
- (17) C-R. Chang, B. Long, X-F. Yang, J. Li, *J. Phys. Chem. C* 119 (2015) 16072-16081.
- (18) Q. Gu, P. Sautet, C. Michel, *ACS Catal.* 8 (2018) 11716-11721.
- (19) A. Abad, P. Concepcion, A. Corma, H. Garcia, *Angew. Chem. Int. Ed* 44 (2005) 4066-4069.
- (20) P. Liu, J. K. Nørskov, *Phys. Chem. Chem. Phys.* 3 (2001) 3814-3818.
- (21) D. Yuan, X. Gong, R. Wu, *Phys. Rev. B* 75 (2007) 233401.
- (22) L. Prati, A. Villa, F. Porta, D. Wang, D-S. Su, *Catal. Today* 122 (2007) 386-390.
- (23) G. J. Hutchings, C. J. Kiely, *Accounts Chem. Res.* 46 (2013) 1759-1772.
- (24) D. Wang, A. Villa, F. Porta, L. Prati, D. Su, *J. Phys. Chem. C* 112 (2008) 8617-8622.

- (25) A. M. Ruppert, M. Jedrzejczyk, N. Portrzebowska, K. Kazmierczak, M. Brzezinska, O. Sneka-Platek, P. Sautet, N. Keller, C. Michel, J. Grams, *Catal. Sci. Technol.* 9 (2018) 4318-4331.
- (26) C. L. Bracey, P. R. Ellis, G. J. Hutchings, *Chem. Soc. Rev.* 38 (2009) 2231-2243.
- (27) J-Q. Goh, J. Akola, R. Ferrando, *J. Phys. Chem. C* 121 (2017) 10809-10816.
- (28) P. Dstro, T. M. Kokumai, A. Scarpellini, L. Pasquale, L. Manna, M. Colombo, D. Zanchet, *ACS Catal.* 8 (2018) 1031-1037.
- (29) A. Sandoval, C. Louis, R. Zanella, *Appl. Catal. B: Environ.* 140-141 (2013) 363-377.
- (30) L. Ma, M. Melander, T. Weckman, K. Laasonen, J. Akola, *J. Phys. Chem. C* 120 (2016) 26747-26758.
- (31) C. D. Pina, E. Falletta, M. Rossi, *J. Catal.* 260 (2008) 384-386.
- (32) T. Pasini, M. Piccinini, M. Blosi, R. Bonelli, S. Albonetti, N. Dimitratos, J. A. Lopez-Sanchez, M. Sankar, Q. He, C. J. Kiely, G. J. Hutchings, F. Cavani, *Green Chem.* 13 (2011) 2091-2099.
- (33) S. Albonetti, T. Pasini, A. Lolli, M. Blosi, M. Piccinini, N. Dimitratos, J. A. Lopez-Sanchez, D. J. Morgan, A. F. Carley, G. J. Hutchings, F. Cavani, *Catal. Today* 195 (2012) 120-126.
- (34) L. Zhang, H. Y. Kim, G. Henkelman, *J. Phys. Chem. Lett.* 4 (2013) 2943-2947.
- (35) K-I. Koizumi, K. Nobusada, M. Boero, *J. Phys. Chem. B* 119 (2015) 15421-15427.
- (36) N. Decker, O. Franke, U. Prüsse, A. Stankowiak, K-D. Vorlop, EP 2146947B1, 2006.
- (37) K. Heidkamp, N. Decker, U. Prüße, *Catal. Commun.* 40 (2013) 88-92.
- (38) K. Heidkamp, M. Aytemir, K-D. Vorlop, U. Prüße, *Catal. Sci. Technol.* 3 (2013) 2984-2992.
- (39) K. Sha, E-J. Zhen, W-J. Zhou, A. Liebens, M. Pera-Titus, *J. Catal.* 337 (2016) 199-207.
- (40) G. Kresse, J. Hafner, *Phys. Rev. B* 47 (1993) 558-561.
- (41) G. Kresse, J. Furthmüller, *J. Comput. Mater. Sci.* 6 (1996) 15-50.
- (42) G. Kresse, J. Furthmüller, *J. Phys. Rev. B* 54 (1996) 11169-11186.
- (43) J. P. Perdew, K. Burke, M. Ernzerhof, *Phys. Rev. Lett.* 77 (1996) 3865-3868.
- (44) S. N. Steinmann, C. Corminboeuf, *J. Chem. Phys.* 134 (2011) 044117.
- (45) G. Kresse, D. Joubert, *Phys. Rev. B* 59 (1999) 1758-1775.
- (46) D. R. Lide, *CRC Handbook of Chemistry and Physics*, 84<sup>th</sup> Edition, 2003.
- (47) K. Letchworth-Weaver, T. A. Arias, *Phys. Rev. B* 86 (2012) 075140.
- (48) D. Gunceler, K. Letchworth-Weaver, R. Sundararaman, K. A. Schwarz, T. A. Arias, *Model. Simul. Mater. Sci. Eng.* 21 (2013) 074005.
- (49) K. Mathew, R. G. Hennig, *ArXiv e-prints* (2016) 1601.03346.

- (50) K. Mathew, R. Sundararaman, K. Letchworth-Weaver, T. A. Arias, R. G. Hennig, *J. Chem. Phys.* 140 (2014) 084106.
- (51) S. N. Steinmann, P. Sautet, *J. Phys. Chem. C* 120 (2016) 5619-5623.
- (52) G. Henkelman, B. P. Uberuaga, H. A. Jónsson, *J. Chem. Phys.* 113 (2000) 9901-9904.
- (53) P. Fleurat-Lessard, P. Dayal, P. Freely available at: <http://forge.cpb.enslyon.fr/redmine/projects/openpath/wiki/WikiEnglish>].
- (54) D. H. Wertz, *J. Am. Chem. Soc.* 102 (1980) 5316-5322.
- (55) S. Karanjit, K. Bobuatong, R. Fukuda, M. Ehara, H., Sakurai, *Int. J. Quantum Chem.* 113 (2013) 428-436.
- (56) M. Okumura, Y. Kitagawa, M. Haruta, K. Yamaguchi, *Chem. Phys. Lett.* 346 (2001) 163-168.
- (57) S. Nishimura, Y. Yakita, M. Katayama, K. Higashimine, K. Ebitani, *Catal. Sci. Technol.* 3 (2013) 351-359.
- (58) P. Wang, S. N. Steinmann, G. Fu, C. Michel, P. Sautet, *ACS Catal.* 7 (2017) 1955-1959.
- (59) B. Thapa, H. B. Schlegel, *J. Phys. Chem. A* 121 (2017) 4698-4706.
- (60) M. V. Fedotova, S. E. Kruchinin, *J. Mol. Liq.* 164 (2011) 201-206.
- (61) C. G. Zhan, D. A. Dixon, *J. Phys. Chem. A* 106 (2002) 9737-9744.
- (62) C. Michel, J. Zaffran, A. M. Ruppert, J. Matras-Michalska, M. Jedrzejczyk, J. Grams, P. Sautet, *Chem. Commun.* 50 (2014) 12450-12453.
- (63) J. Zaffran, C. Michel, F. Delbecq, P. Sautet, *Catal. Sci. Technol.* 6 (2016) 6615-6624.
- (64) F. Le Normand, L. Hilaire, K. Kili, G. Krill, G. Maire, *J. Phys. Chem.* 92 (1988) 2561-2568.
- (65) A. Kotani, T. Jo, J. C. Parlebas, *Adv. Phys.* 37 (1988) 37-85.
- (66) A. Laachir, V. Perrichon, A. Badri, J. Lamotte, E. Catherine, J. C. Lavalley, J. El Fallah, L. Hilaire, F. le Normand, E. Quemere, G. N. Sauvion, O. Touret, *J. Chem. Soc., Faraday Trans.* 87 (1991) 1601-1609.
- (67) A. Zwijnenburg, A. Goosens, W. G. Sloof, M. W. J. Graje, A. M. Kraan, L. J. de Jongh, M. Makkee, J. A. Moulijn, *J. Phys. Chem. B* 106 (2002) 9853-9862.
- (68) N. Dimitratos, A. Villa, C. L. Bianchi, L. Prati, M. Makkee, *Appl. Catal. A: Gen.* 311 (2006) 185-192.
- (69) J. Radnik, C. Mohr, P. Claus, *Phys. Chem. Chem. Phys.* 5 (2003) 172-177.
- (70) R. J. Chimentão, F. Medina, J. L. G. Fierro, J. Llorca, J. E. Sueiras, Y. Cesteros, P. Salagre, *J. Mol. Catal. A: Chem.* 274 (2007) 159-168.



- (71) C. D. Wagner, W. M. Riggs, L. E. Davis, J. F. Mouler, Handbook of X-Ray Photoelectron Spectroscopy; G. E. Muilenberg, ed, Perkin Elmer Corporation, Physics Electronics Division: Eden Prairie, MN, 1979.
- (72) C. C. Chusuei, M. A. Brookshier, D. W. Goodman, *Langmuir* 15 (1999) 2806-2808.
- (73) A. F. Carley, L. A. Dollard, P. R. Norman, C. Pottage, M. W. Roberts, *J. Electron. Spectr. Related Phenom.* 98-99 (1999) 223-233.
- (74) C-K. Wu, M. Yin, S. O'Brien, J. T. Koberstein, *Chem. Mater.* 18 (2006) 6054-6058.
- (75) S. Kozuch, S. Shaik, *Acc. Chem. Res.* 44 (2011) 101-110.